

**UCLA**

**UCLA Electronic Theses and Dissertations**

**Title**

Dynamic Analysis of Thin Film Multiferroic Radiation via FDTD Methods

**Permalink**

<https://escholarship.org/uc/item/32x6m6sq>

**Author**

Yao, Zhi

**Publication Date**

2014

Peer reviewed|Thesis/dissertation

UNIVERSITY OF CALIFORNIA

Los Angeles

**Dynamic Analysis of Thin Film Multiferroic  
Radiation via FDTD Methods**

A thesis submitted in partial satisfaction  
of the requirements for the degree  
Master of Science in Electrical Engineering

by

**Zhi Yao**

© Copyright by

Zhi Yao

2014

ABSTRACT OF THE THESIS

# **Dynamic Analysis of Thin Film Multiferroic Radiation via FDTD Methods**

by

**Zhi Yao**

Master of Science in Electrical Engineering

University of California, Los Angeles, 2014

Professor Yuanxun Wang, Chair

A bulk acoustic wave (BAW) based multiferroic antenna structure is proposed, to overcome the platform effect associated with low-profile antennas. Numerical analysis based on the one-dimensional finite-difference time-domain (1D FDTD) technique, as well as analytical analysis is applied. The dynamic stress profile within the resonator and the radiation quality factors (Q factors) are simulated. The radiation of the electromagnetic waves acting as a damping load to the acoustic resonances is represented. In addition, both electrical conductive loss of nickel and magnetic damping loss of yttrium iron garnet (YIG) are considered and simulated with full dynamics via the coupling of Maxwell's equations and Landau-Lifshitz-Gilbert (LLG) equations. In the LLG/Maxwell modeling, the simulated relative permeability curves match the theoretical plot obtained by classical analysis. Furthermore, the radiated power is simulated, which increases as the thickness of the film increases or the line width of the material decreases. It should be noted that the normalized radiation power is maximum at the ferromagnetic resonance frequency (FMR), which opens up a new antenna design strategy to make the antenna work at FMR to enhance the radiation. The agreement between the numerical solutions and the analytical solutions provides a validation to the operating principle of the proposed antenna.

The thesis of Zhi Yao is approved.

Tatsuo Itoh

Yahya Rahmat-Samii

Yuanxun Wang, Committee Chair

University of California, Los Angeles

2014

## TABLE OF CONTENTS

<b>Introduction .....</b>	<b>1</b>
1.1. Radiation Quality Factor of Low Profile Antennas .....	1
1.2. Platform Effect for Current Based Antennas .....	3
1.3. Thesis Outline .....	4
<b>Multiferroic Based Dynamic System .....</b>	<b>5</b>
2.1. Multiferroics.....	5
2.1.1. Multiferroic Materials.....	5
2.1.2. Multiferroic Radiation .....	6
2.2. Strain-mediated Multiferroics and Constitutive Coupling.....	7
2.3. Lower Bound in Radiation Q factor .....	10
<b>One-dimensional FDTD Dynamic Analysis .....</b>	<b>13</b>
3.1. BAW Resonance Based Thin-film Antenna .....	13
3.1.1. Proposed Antenna Structure .....	13
3.1.2. Material Requirements.....	15
3.2. FDTD Dynamic Modeling of the BAW Antenna .....	16
3.2.1. Difference Equations .....	16
3.2.2. Modeling Results and Analysis.....	19
<b>Identification of Loss Effects.....</b>	<b>23</b>
4.1. Eddy Current Loss.....	23
4.2. Magnetic Damping Loss.....	25

4.2.1. Modeling Setup.....	25
4.2.2. Modeling Result and Analysis .....	27
<b>CHAPTER 5 .....</b>	<b>31</b>
5.1. Summary .....	31
5.2. Future Work.....	31
<b>APPENDIX A.....</b>	<b>32</b>
<b>APPENDIX B.....</b>	<b>34</b>
<b>REFERENCES .....</b>	<b>38</b>

## LIST OF FIGURES

1.1.1.	Radiation platform effect of thin-film antennas .....	2
1.2.1.	Current source working as radiating element .....	3
2.1.1.	(a) Relationship between multiferroic and magnetoelectric materials. Illustrates the requirements to achieve both in a material. (b) Schematic illustrating different types of coupling present in materials. ....	6
2.1.2.	Simple model of multiferroic radiation.....	6
2.2.1.	Strain mediated radiation in the magnetostrictive layer.....	8
2.3.1.	Parallel circuit model of strain mediated radiation in the magnetostrictive layer.....	12
3.1.1.	BAW resonance based antenna. ....	14
3.1.2.	The proposed structure expanded to different thicknesses.....	14
3.2.1.	Time-domain stress field within the antenna with geometry by Fig. 3.1.1, with ideal nickel with no loss as the magnetostrictive material.....	20
3.2.2.	(a) Simulated radiation $Q$ compared to the theory for different permeability, $k_H = 0.85$ . (b) Simulated radiation $Q$ compared to the theory for different magnetic to mechanical figure of merits, $\mu_r = 2000$ . The parameters in Fig. 3.2.1 apply.....	20
3.2.3.	Stress profiles inside the proposed antenna structure of Fig. 3.1.1.....	21
4.1.1.	Figure. 4.1.1. Stress curves with different conductivity.....	24
4.2.1.	Problem statement.....	26



4.2.2. 1D leap-frogging procedure.....	27
4.2.3. Time domain field profiles.....	28
4.2.4. Relative permeability as a function of frequency.....	28
4.2.5. Relative permeability curves with various values of DC bias.....	29
4.2.6. Normalized radiated power.....	30

## LIST OF TABLES

3.1.1.	Material candidates for piezoelectric material.....	15
3.1.2.	Material candidates for magnetostrictive material.....	15
4.1.1.	Quality factors with different conductivities.....	25

## ACKNOWLEDGMENTS

I would like to express my special thanks of gratitude to my advisor, Dr. Yuanxun Wang, for his professional guidance and valuable support throughout this work. I am also grateful to Dr. Qiang Xu, who had many helpful discussions with me regarding this work, and Dr. Xi Yang, for his useful and constructive recommendations on this work. In addition, I would like to express my gratitude to Center for Translational Applications of Nanoscale Multiferroic Systems (TANMS) at UCLA, funded by National Science Foundation, for the financial and knowledge support. I also thank Professor Tatsuo Itoh and Professor Yahya Rahmat-Samii for their kindness of reviewing this thesis. It is a great honor for me to have them serve as my thesis committee.

# CHAPTER 1

## Introduction

Nowadays, the demand for small antennas has become an important consideration of antenna engineers. However, the desire for electrically small antennas is obstructed by various technical issues. One of the dominant problems is the platform effect. In this work, we do not deal with electrically small antennas, instead, we look at thin-film (or low-profile) antennas, to solve the problem of platform effect. Traditional current based antennas suffer the platform effect when placed at a short distance above a conducting plane [1]. The radiation becomes inefficient as the image current flowing in the opposite direction and canceling the radiation. The excessive storage of reactive energy between the radiating element and the conducting plane raises the radiation quality factor (Q factor) [2]. On the other hand, creating electromagnetic radiation through mechanical variables such as dynamic strains have been investigated in [5]–[8].

### 1.1. Radiation Quality Factor of Low Profile Antennas

Platform effect is the phenomenon that current based antenna does not radiate efficiently when it is placed very close to an electrically conducting ground (Fig. 1.1.1). The inefficiency of radiation is due to near-cancellation of radiated fields when the current element is in very close proximity to its negative image caused by the presence of the ground plane [11]. Since the original radiated field and the reflected field by the ground form a strong standing wave beneath the current source, platform effect also causes excessive storage of reactive energy between the radiating element and the conducting plane.

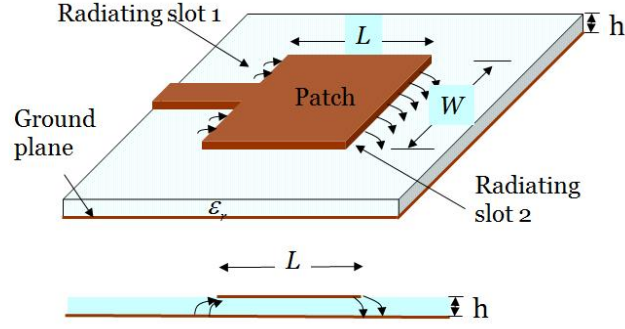


Figure. 1.1.1: Radiation platform effect of thin-film antennas. Note that in this work, we do not deal with electrically small antennas, instead, we look at thin-film (or low-profile) antennas, to solve the problem of platform effect.

The ability of an antenna to radiate is usually described by radiation  $Q$  factor. Radiation  $Q$  factor denotes the ratio of the average stored energy within the antenna structure to the radiated power per cycle, which is defined as:

$$Q_{rad} = \omega \frac{(\text{average energy stored})}{(\text{radiated power})} = \omega \frac{W_e + W_m}{P_{rad}} \quad (1.1.1)$$

where  $W_e$  and  $W_m$  are the total electric energy and magnetic energy stored in the structure, respectively,  $P_{rad}$  is the radiated power, and  $\omega$  is the angular frequency that the system works at. Based on the definition, lower radiation  $Q$  factor leads to better antenna radiation performance. Chu [3] and Mclean [4] evaluated the theoretical radiation  $Q$  factor lower bound of antennas, which is the fundamental limit of the radiation performance of all antennas. The platform effect can be observed from the elevated radiation  $Q$  factor as a great amount of energy is required to be stored between the radiating element and the conducting platform before a reasonable amount of power can be radiated [2]. The high radiation  $Q$  factor caused by platform effect also affects the radiation efficiency which becomes more sensitive to ohmic loss and dielectric loss. The radiation efficiency is given by

$$\xi_r = \frac{Q_{diss}}{Q_{rad} + Q_{diss}} \approx \frac{Q_{diss}}{Q_{rad}}, \text{ when } Q_{diss} \ll Q_{rad} \quad (1.1.2)$$

where  $Q_{diss}$  is the dissipation  $Q$  factor. As  $Q_{rad}$  increases, the radiation efficiency becomes lower and the influence of  $Q_{diss}$  becomes more dominant.

## 1.2. Platform Effect for Current Based Antennas

Consider an infinite, uniform current sheet that radiates into free space backed by an infinite perfect electrically conducting (PEC) ground plane (Fig. 1.2.1). The thickness of the substrate is electrically small so that  $kh \ll 1$ . The wave directly radiated into the free space and the one reflected by the PEC plane interfere with each other in space and thus create a standing wave in the substrate. The electromagnetic waves in different region are:

$$\begin{aligned} \text{Energy storage field} \quad & \begin{cases} E_x = E_0 \sin kz \\ H_y = E_0 / j\eta \cos kz \end{cases} \quad z < h \\ \text{Radiated field} \quad & \begin{cases} E_x = E_0 \sin kh \exp(-jk_0 z) \\ H_y = E_0 / \eta_0 \sin kh \exp(-jk_0 z) \end{cases} \quad z > h \end{aligned} \quad (1.2.1)$$

where  $E_0$  is the aperture electric field amplitude at the interface between the free space and the substrate.

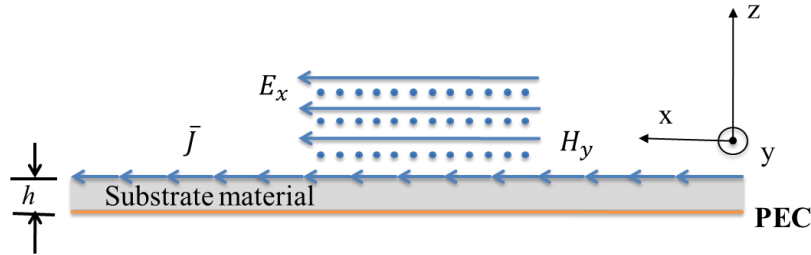


Figure. 1.2.1: Current source working as radiating element. The coordinate system is chosen such that the surface current is in the  $x$  direction. The thickness of the substrate satisfies the condition  $kh \ll 1$ .

The radiated power into the free space is

$$P_{rad} = \frac{1}{2\eta_0} \iint_s |E|^2 ds \approx \frac{1}{2\eta_0} E_0^2 (kh)^2 S \quad (1.2.2)$$

In (1.2.2), an approximation of linear electric field distribution along  $z$  direction is used. Similarly,

an approximation of uniform magnetic field distribution along  $z$  direction leads to:

$$W_H = \frac{1}{2} \iiint_{z < h} \mu |H|^2 dv \approx \frac{1}{2} \mu |H|^2 hS = \frac{1}{2} \varepsilon E_0^2 hS \quad (1.2.3)$$

Since  $W_E \ll W_H$ , the electric energy stored in the structure is negligible, thus  $W_T \approx W_H$ , which results in:

$$Q_{rad} = \omega \frac{W_H}{P_{rad}} = \frac{1}{\mu_r k_0 h} = \frac{\lambda_0}{2\pi h} \frac{1}{\mu_r} \quad (1.2.4)$$

Hence, for an antenna working at  $1GHz$ ,  $Q_{rad}$  is on the order of  $10^4$  when the thickness of the substrate is  $2\mu m$  if the material is non-magnetic. Since traditional antennas are mostly made of conductors and rely on conductive current to radiate, platform effect is an inevitable shortcoming of traditional low-profile antennas.

### 1.3. Thesis Outline

In this work, a bulk acoustic wave (BAW) based multiferroic antenna structure is proposed, which consists of a sandwich of two layers of piezoelectric material and one layer of thin film magnetostrictive material. Analysis shows that with high permeability and high mechanical-magnetic coupling factor, the platform effect can be well suppressed, which could lead to low profile antennas with low radiation Q factor and high radiation efficiency. In addition, a one-dimensional (1D) finite-difference time-domain (FDTD) technique [9, 10] is developed for dynamic simulations of the proposed antenna structure by solving Newton's law and Maxwell's equations jointly. The dynamic variation of the stress profile and the radiation Q factor is presented, with agreement to the analytical results.

## CHAPTER 2

### Multiferroic Based Dynamic System

Although traditional current excited low-profile antennas could barely get rid of platform effect, it is prospective to replace the electric current with other types of excitation and very likely to avoid platform effect of thin-film antennas. Strain mediated multiferroic materials have shown the promise of creating electromagnetic radiation through strain induced magnetization reorientation. In this chapter, the physics inside the multiferroic radiation is investigated, and the fundamental limit on the radiation Q factor of the thin-film multiferroic radiation is derived.

#### 2.1. Multiferroics

##### 2.1.1. Multiferroic Materials

Schmid coins the term “multiferroic” in 1994 [12]; since then, thousands of papers have been published investigating the attractive properties of this type of material. Multiferroic materials are materials that exhibit at least two, and sometimes all three, types of ferroic ordering in the same phase. The ferroic orderings are ferroelectric, ferromagnetic and ferroelastic and relate to the type of applied field required for the material to exhibit a spontaneously polarized state.

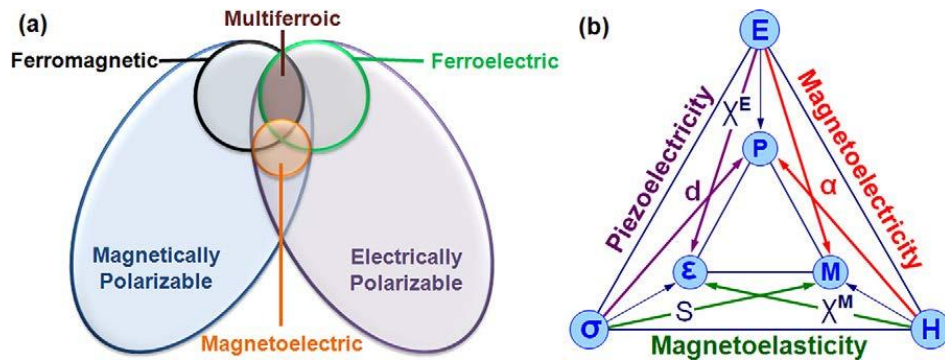




Figure. 2.1.1: (a) Relationship between multiferroic and magnetoelectric materials. Illustrates the requirements to achieve both in a material. (b) Schematic illustrating different types of coupling present in materials. Much attention has been given to materials where electric and magnetic order is coupled. These materials are known as magnetoelectric materials. [13]

Fig. 2.1.1 shows these types of ferroic ordering, where an applied electric, magnetic or stress field induces a spontaneous electric polarization, magnetization or strain, respectively [13]. However, in multiferroics additional levels of ordering can result from the coupling between the different types of ferroic ordering. For instance, in a magnetoelectric multiferroic, an applied magnetic field can be used to control the polarization, or an applied electric field could be used to control the magnetization.

### 2.1.2. Multiferroic Radiation

Composite multiferroics typically consist of alternating layers of piezoelectric and magnetostrictive materials [13, 16]. Piezoelectric and magnetostrictive materials undergo a shape change in an applied electric or magnetic field, respectively. The coupling in these materials is mechanical in nature. Multiferroic radiation is thus the radiation via multiferroic interactions among electric, magnetic, and mechanical property of the material. Fig. 2.1.2 shows an example of multiferroic radiation using composite multiferroics.

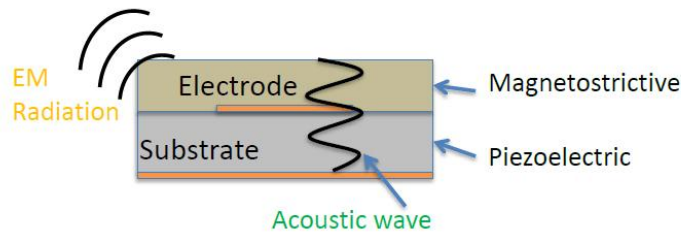


Figure. 2.1.2: Simple model of multiferroic radiation

The obvious advantages of multiferroic radiation devices over the traditional ones are listed as follows:

1. New field generation mechanism:

- Coupling mechanisms compatible with the platform. The bulk acoustic wave (BAW) based multiferroic radiating elements allow efficient coupling between the ferroelectric phase and the ferromagnetic phase in the vertical dimension, while retaining the ability to be scaled in the other two horizontal dimensions for practical antenna applications.
- Loss characteristics scaling favors smaller dimension.

2. Wavelength transformation

- Resonance based matching elements at the scale of five orders of magnitude smaller, due to the fact that acoustic wavelength is five orders of magnitude smaller than the electromagnetic wavelength.
- Leverage on thin film material or nanofabrication techniques. Thin film materials usually exhibit better property manipulations than the bulk materials.

## 2.2. Strain-mediated Multiferroics and Constitutive Coupling

The electromagnetic radiation into free space is determined by Maxwell's equations (2.2.1):

$$\nabla \times \bar{E} = -\frac{\partial \bar{B}}{\partial t}, \quad \nabla \times \bar{H} = \sigma \bar{E} + \frac{\partial \bar{D}}{\partial t} \quad (2.2.1)$$

where  $\bar{E}$  and  $\bar{H}$  are the electric and magnetic field intensity vectors,  $\bar{D}$  and  $\bar{B}$  are the electric and magnetic flux density vectors,  $\sigma$  is the conductivity of the material that the antenna is made of,  $\sigma \bar{E}$  is the conductive current source. In this chapter and Chapter 3,  $\sigma$  is assumed to be zero so that the magnetostrictive material is electrically lossless. According to Eq. (2.2.1), besides the conductive current, both  $\bar{D}$  and  $\bar{B}$  may be utilized to create electromagnetic radiation. This requires magnetoelectric coupling, which in turn relies on magnetoelectric multiferroic materials, where the simultaneous presence of, and the coupling between, magnetic and electric orders exist [14, 15]. Composite strain-mediated multiferroic material system utilizes strain field, i.e. crystal deformation, to couple between the ferroelectric phase (via piezoelectric effect) and the magnetic

phase (via magnetostriction) [14]. When a voltage or current is used to excite the composite, the converse piezoelectric effect leads to a stress in the magnetic phase, which induces the reorientation of the magnetization via magnetoelastic interactions [16]. Due to the ability of thin-film piezoelectric and magnetostrictive materials to generate strong strain coupled electric and magnetic flux and therefore to enable the radiation of electromagnetic waves, such materials have shown the promise of creating electromagnetic radiation through mechanical-electromagnetic coupling.

In order to understand the response of multiferroic interactions among electric, magnetic and mechanical properties of the material with a focus on small scale element interactions and its dynamic and frequency characteristics, the strain mediated radiation model (Fig. 2.2.1) is analyzed. For simplification, only the thin-film magnetostrictive layer is included in Fig. 2.2.1, since it works as the radiating element among the multiferroic composite. Strain field coupled from the piezoelectric layer is applied in the vertical direction, forming a BAW resonance which in turn maximizes the coupling of the strain field. Through mechanical-magnetic coupling, a time-variant in-plane magnetic flux density  $\bar{B}$  is generated within the layer, which simultaneously generates a time-variant aperture  $\bar{E}$  field, thus electromagnetic radiation is created.

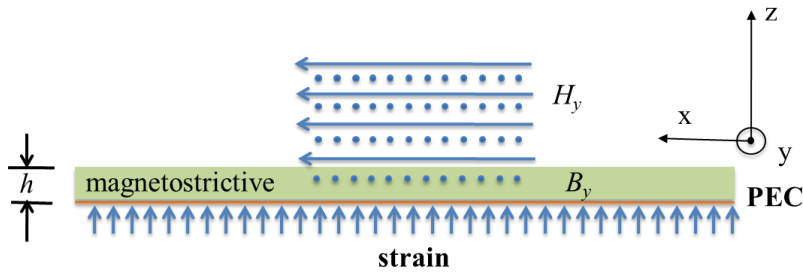


Figure. 2.2.1: Strain mediated radiation in the magnetostrictive layer. The coordinate system is chosen such that the surface current is in the  $x$  direction. The thickness of the substrate satisfies the condition  $kh \ll 1$ .

In a multiferroic system, electromagnetic waves are determined by Maxwell's equations (2.2.1), and the behavior of acoustic waves is governed by Newton's laws (2.2.2). The two dynamic systems are related by the multiferroic constitutive coupling equations (2.2.3), (2.2.4) [17].

$$\nabla \cdot \bar{T} = \rho \frac{\partial \bar{v}}{\partial t}, \quad \nabla_s \bar{v} = \frac{\partial \bar{S}}{\partial t} \quad (2.2.2)$$

$$\bar{S} = \begin{bmatrix} s_E \\ s_H \end{bmatrix} \bar{T} + \begin{bmatrix} d_E \\ d_H \end{bmatrix} \begin{bmatrix} \bar{E} \\ \bar{H} \end{bmatrix} \quad (2.2.3)$$

$$\begin{bmatrix} \bar{D} \\ \bar{B} \end{bmatrix} = \begin{bmatrix} d_E \\ d_H \end{bmatrix} \bar{T} + \begin{bmatrix} \varepsilon_T \\ \mu_T \end{bmatrix} \begin{bmatrix} \bar{E} \\ \bar{H} \end{bmatrix} \quad (2.2.4)$$

In Eq. (2.2.3) and (2.2.4), the equations in the first row are the piezoelectric strain equations, and those in the second row are the magnetostrictive strain equations. The terms  $\bar{T}$  and  $\bar{S}$  stand for the stress and strain tensors,  $\bar{v}$  is the particle velocity vector,  $\rho$  is the mass density of the material. In the piezoelectric strain equations,  $\varepsilon_T$  is the piezoelectric permittivity,  $s_E$  is the piezoelectric compliance constant, and  $d_E$  is the piezoelectric strain constant. Subscripts  $T$  and  $E$  have been added to  $\varepsilon$  and  $s$  to show that these coefficients describe dielectric and elastic properties measured under conditions of constant stress and constant electric field, respectively [17]. In the magnetostrictive strain equations,  $\mu_T$  is the magnetostrictive permeability,  $s_H$  is the magnetostrictive compliance constant, and  $d_H$  is the magnetostrictive strain constant. Similarly, the subscripts  $T$  and  $H$  added to  $\mu$  and  $s$  show that these coefficients describe magnetic and elastic properties measured under conditions of constant stress and constant magnetic field, respectively.

Due to the thin-film profile, both the magnetostrictive and piezoelectric layers are assumed to have uniform strain and stress field distribution in plane. The material is also assumed to be isotropic and uniform in plane. Therefore, the strain equations in (2.2.3) and (2.2.4) reduce to

$$S = s_E T + d_E E, \quad D = d_E T + \varepsilon_T E \quad (2.2.5)$$

$$S = s_H T + d_H H, \quad B = d_H T + \mu_T H \quad (2.2.6)$$

Equation (2.2.5) is piezoelectric strain equations and (2.2.6) is magnetostrictive strain equations.

Furthermore, the stress equations can be derived from (2.2.5)–(2.2.6):

$$T = -\frac{e_D}{\varepsilon_S} D + c_D S, E = \frac{1}{\varepsilon_S} D - \frac{e_D}{\varepsilon_S} S \quad (2.2.7)$$

$$T = -\frac{e_B}{\mu_S} B + c_B S, H = \frac{1}{\mu_S} B - \frac{e_B}{\mu_S} S \quad (2.2.8)$$

where  $e_B$  is the stress constant of the magnetostrictive material, which is defined as

$e_B = d_H / s_H = d_H \cdot c_H$ . The coefficient  $c_H$  is the Young's modulus of the material,  $c_H = 1/s_H$ . The

coefficients  $c_B$  and  $\mu_S$  are defined as following:

$$c_B = \frac{c_H}{1 - k_H^2}, \mu_S = \mu_T (1 - k_H^2) \quad (2.2.9)$$

$$k_H^2 = \frac{d_H^2}{s_H \mu_T} \quad (2.2.10)$$

In (2.2.10),  $k_H^2$  is the mechanical-to-magnetic figure of merit. The physical significance of  $k_H^2$  will be interpreted in the following paragraph. The piezoelectric parameters are defined in the same way.

### 2.3. Lower Bound in Radiation Q factor

As illustrated previously, BAW based multiferroic system shows the potential of suppressing platform effect associated with low-profile antennas. Since platform effect results in high radiation Q factor, a low radiation Q factor indicates well suppression of the platform effect. To demonstrate this capacity of multiferroic antenna, the lower bound of radiation Q factor needs to be derived.

The total stored energy  $w_T$  in the system is given by:

$$\begin{aligned} W_T &= \frac{1}{2} \iiint_{z < h} S \cdot T dv + \frac{1}{2} \iiint_{z < h} B \cdot H dv \\ &= \frac{1}{2} \iiint_{z < h} s_B |T|^2 dv + \frac{1}{2} \iiint_{z < h} \frac{|B|^2}{\mu_T} dv \end{aligned} \quad (2.3.1)$$

When the system has a high radiation  $Q$  factor,  $H$  field is approximately zero in Eq. (2.3.1). This approximation is valid since the analysis is executed on an antenna with a new working mechanism which would otherwise have poor performance. Therefore

$$W_T = W_{ME} = \frac{1}{k_H^2} \frac{1}{2} \iiint_{z < h} \frac{|B|^2}{\mu_T} dv = \frac{1}{k_H^2} W_H \quad (2.3.2)$$

Note that because the input energy to the radiating element is the mechanical energy,  $W_T$  could be substituted by  $W_{ME}$ . The term  $k_H^2$ , defined by (2.2.10), is the mechanical-magnetic figure of merit, i.e., the maximum ratio of mechanical energy transferred to magnetic energy in the form of magnetic flux density. The fundamental limit for  $k_H^2$  is  $k_H^2 \leq 1$ . The expressions of the radiated power and the stored magnetic energy are given by Eq. (2.3.3) and (2.3.4).

$$P_{rad} = \frac{1}{2\eta_0} \iint_s |E_0|^2 ds \quad (2.3.3)$$

$$W_H = \frac{1}{2} \iiint_{z < h} \frac{|B|^2}{\mu_T} dv \approx \frac{h}{2(\omega h)^2 \mu_T} \iint_s |E_0|^2 ds \quad (2.3.4)$$

Note that in the process of deriving (2.3.3) and (2.3.4) we made the following extrapolation approximation

$$B_x = B_{x0}, H_x = H_{x0}, E_y = E_{y1}z \quad (2.3.5)$$

to overcome the stability problem, which is non-negligible in the finite difference time domain (FDTD) modeling to be introduced in Chapter. 3. For details, see Section 3.1. *BAW Resonance Based Antenna Structure*, Chapter 3.

$$Q_{bound} = \omega \frac{W_{ME}}{P_{rad}} = \omega \frac{W_H / k_H^2}{P_{rad}} = \frac{1}{k_H^2} \frac{1}{\mu_r k_0 h} = \frac{s_H}{d_H^2} \frac{\mu_0}{k_0 h} \quad (2.3.6)$$

The lower bound of the radiation  $Q$  factor, given by (2.3.6) from definition (1.1.1), indicates that with high permeability and high mechanical-to-magnetic coupling factor of the thin film magnetic material, the platform effect can be well suppressed, which could lead to extremely low profile

antennas with low radiation  $Q$  factor and high radiation efficiency. Again, the figure of merit  $k_H^2$  indicates the maximum ability of the multiferroic system to transfer mechanical energy into electromagnetic energy.

As a supplement analysis, the radiation into free space is modeled as a damping load to the acoustic resonator, shown by the circuit model of Fig. 2.3.1.

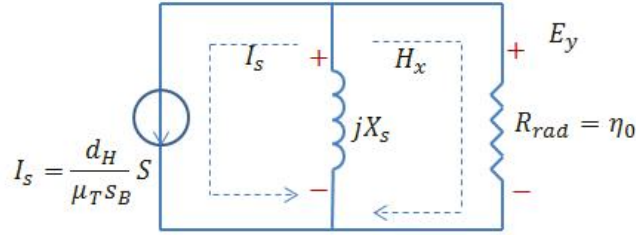


Figure. 2.3.1: Parallel circuit model of strain mediated radiation in the magnetostrictive layer. The BAW resonance is modeled as an inductor with inductance of  $X_s$ , and the radiation into free space is modeled as a pure resistor with a resistance of  $R_{rad}$ . The radiated electric field is modeled as the voltage over the

damping load,  $E_y = -jX_s \left[ \frac{d_H S}{\mu_T S_H (1 - k_H^2)} + H_x \right]$ , where  $X_s = \omega h \mu_T (1 - k_H^2)$ . For thin material, the

thickness of the layer  $h$  is very small, thus  $X_s \ll R_{rad}$ . The validation of radiation acting as a damping load will be presented in Chapter 3.

## CHAPTER 3

### One-dimensional FDTD Dynamic Analysis

The BAW based multiferroic radiating elements allow efficient coupling between the ferroelectric phase and the ferromagnetic phase in the vertical dimension, while retaining the ability to be scaled in the other two horizontal dimensions for practical antenna applications. A three-layer multiferroic structure with bulk acoustic waves as strain media is proposed to achieve the vertical multiferroic coupling in addition to the horizontal scalability. An air cavity or brag reflector such as those in film bulk acoustic wave resonator (FBAR) can be used to overcome the clamping effect of the substrate.

#### 3.1. BAW Resonance Based Thin-film Antenna

##### 3.1.1. Proposed Antenna Structure

Fig. 3.1.1 shows the proposed BAW based multiferroic antenna structure, with a  $1\text{-}\mu\text{m}$ -thick magnetostrictive layer sandwiched by two  $1\text{-}\mu\text{m}$ -thick piezoelectric layers. The bottom piezoelectric layer serves as the excitation layer which injects the acoustic waves into the layered structure. Vertical BAW resonance is formed and it can maximize the strain coupled to the magnetostrictive layer at the resonating frequency. A total of  $3\text{-}\mu\text{m}$ -thick layered structure allows the scaling up of the resonance frequency to approximately  $1\text{GHz}$ . The structure can be expanded to multilayer vertically and to larger dimension horizontally for more efficient radiation. An air cavity or brag reflector such as those in film bulk acoustic wave resonator (FBAR) can be used to overcome the clamping effect of the substrate. An analysis for the energy stored in the sandwiched structure can be performed which includes energy stored in both the magnetostrictive and piezoelectric phase. The stored energy in these two phases is related proportionally by the vertical strain profile in the structure at the resonance. It can thus be derived that



$$Q_a = \omega \frac{2W_{PE} + W_{PM}}{P_{rad}} = \omega \frac{2}{(\sqrt{3}/2\pi + 1/3)} \frac{W_{PM}}{P_{rad}} = \frac{2Q_{bound}}{(\sqrt{3}/2\pi + 1/3)} \quad (3.1.1)$$

where  $W_{PE}$  and  $W_{PM}$  are the stored mechanical energy in each of the piezoelectric layer and magnetic layer and  $Q_{bound}$  is the radiation  $Q$  fundamental limit (2.3.6).

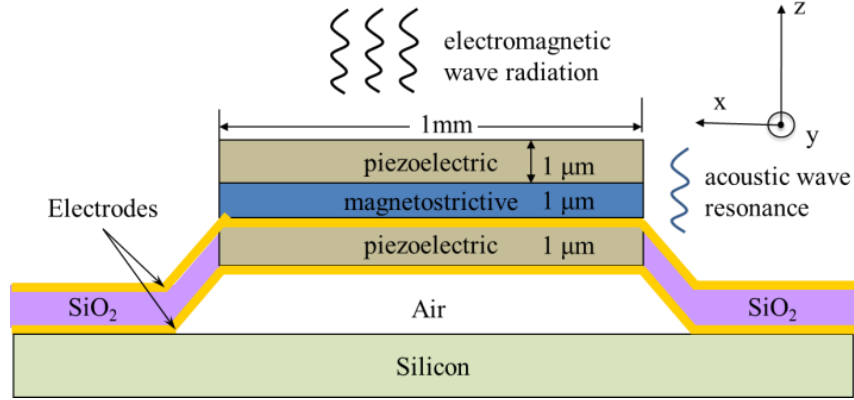


Figure. 3.1.1: BAW resonance based antenna. Electric current excitation is applied to the electrodes on both sides of the bottom piezoelectric layer, and it triggers the BAW resonance through converse piezoelectric effect. Possible choices for the magnetostrictive material is nickel, iron gallium boron, cobalt ferrite, and so on.

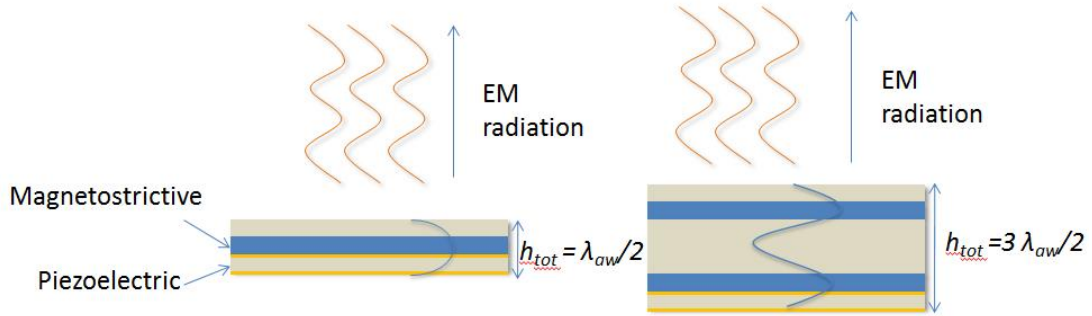


Figure. 3.1.2: The proposed structure expanded to different thicknesses, with the blue curves representing the stress profile inside the structure.

Due to the scalability of the proposed structure, it may be extended vertically to enable different working frequencies, as shown by Fig. 3.1.2. As can be seen from the standing wave profile of the stress field inside the structure, the coupling between the mechanical energy to the magnetic

energy is maximized with the total thickness  $h_{tot} = (n + 1/2)\lambda_{acoustic}$ , since the stress field is maximum in the middle magnetostrictive layer, which serves as the radiating layer. Similarly, we should expect near-zero radiating out of thickness  $h_{tot} = n\lambda_{acoustic}$ , since the stress field is zero in the middle layer. This conjecture will be proved in the next section.

### 3.1.2. Material Requirements

The desired property for antenna of the ferroelectric materials is:

- Mechanically stiff,
- High piezoelectric coefficient,

which leads us to the possible candidates of the material in Table. 3.1.1.

Material	E (GPa)	$d_{33}$ (pC/N)	$V_{sub}$ (m/s)	$\tan \delta$
LiNbO <sub>3</sub>	200	27	3970	.005
PMN-PT	105	1400 - 3500	2336	.01
AlN	250	5.5	5760	.001

Table. 3.1.1. Material candidates for piezoelectric material.

The desired property for antenna of the ferroelectric materials is:

- High permeability, magnetically soft, narrow FMR linewidth,
- High piezomagnetic coefficient

which leads us to the possible candidates of the material in Table. 3.1.2.

Material	Relative $\mu$	Coercivity (Oe)	FMR linewidth (Oe)	Piezomagnetic (ppm/Oe)
Nickel	-	35	~250	0.17
FeGaB	500	<1	~20	7.0
YIG	32	4	~1	.05
Metglas	>80,000 (bulk)	<1	200 (for bulk)	4.0
Terfenol-D	3-10 (bulk)	$0.6 - 2.5 \times 10^3$	~1000	2.8

Table. 3.1.2: Material candidates for magnetostrictive material.

These material properties are derived using coupled elastodynamic models and Maxwell's equations to provide general guidance. Using these material properties the material thrust has begun to narrow down the appropriate thin film magnetic materials. For example, the reported specs for FeGaB is  $M_s=12500$  Oe,  $H_0=20$  Oe, Young's modular's  $Y=55$  GPa, Piezomagnetic coefficient  $dH=7\text{ppm/Oe}$ , which gives a relative permeability  $\mu_r$  of approximately 600 and magnetic-to-mechanical figure of merit of approximately 80%. Therefore the property of FeGaB is very close to the desired range except its conductivity, which needs to be significantly lowered in order to match the requirements.

### 3.2. FDTD Dynamic Modeling of the BAW Antenna

Finite difference time domain (FDTD) method, originally developed by Yee [9], is a powerful numerical approach to model electromagnetic problems with complex structures, as it requires relatively small physical memory and provides physical insight by giving the spatial and temporal results [10]. In this work, a 1D-FDTD code is developed, by solving Maxwell's equations (2.2.1) and Newton's laws (2.2.2) jointly and it predicts the coupling between the acoustic waves and electromagnetic waves through strain mediated constitutive coupling (2.2.3), (2.2.4).

#### 3.2.1. Difference Equations

The combination of (2.2.2) and (2.2.7) leads to 1D differential equations with full dynamics in the piezoelectric layer:

$$\frac{\partial E}{\partial t} = -\frac{e_D}{\epsilon_s} \frac{\partial v}{\partial z} + \frac{1}{\epsilon_s} \frac{\partial D}{\partial t} \quad (3.2.1)$$

$$\frac{\partial T}{\partial t} = c_D \frac{\partial v}{\partial z} - \frac{e_D}{\epsilon_s} \frac{\partial D}{\partial t} \quad (3.2.2)$$

$$\frac{\partial T}{\partial z} = \rho \frac{\partial v}{\partial t} \quad (3.2.3)$$

where the electric flux density  $D$  serves as the excitation. Similarly, the combination of (2.2.2) and (2.2.8) leads to 1D differential equations with full dynamics in the magnetostrictive layer:

$$\frac{\partial H}{\partial t} = -\frac{e_B}{\mu_s} \frac{\partial v}{\partial z} + \frac{1}{\mu_s} \frac{\partial B}{\partial t} \quad (3.2.4)$$

$$\frac{\partial T}{\partial t} = c_B \frac{\partial v}{\partial z} - \frac{e_B}{\mu_s} \frac{\partial B}{\partial t} \quad (3.2.5)$$

$$\frac{\partial T}{\partial z} = \rho \frac{\partial v}{\partial t} \quad (3.2.3)$$

In order to solve (2.2.1) and (2.2.2) simultaneously, the electromagnetic radiation boundary condition and the mechanical dynamics need to be coupled. The spatial basis functions in the magnetostrictive layer are given by

$$B_x = B_{x0}, H_x = H_{x0}, E_y = E_{y1}z \quad (2.3.5)$$

which simplifies Faraday's law in (2.2.1) to

$$\frac{\partial B_x}{\partial t} = \frac{\partial E_y}{\partial z} = E_{y1} \quad (3.2.6)$$

Let us probe into the extrapolation approximation made in Eq. (2.3.5). In time domain numerical modeling, the stability condition between the spatial grid and the time step is

$$\max(\Delta x, \Delta y, \Delta z) \geq \frac{c\Delta t}{\sqrt{3}} \quad (3.2.7)$$

to stabilize the iteration process. In this problem, the proposed thickness of the radiating magnetostrictive thin film is  $1\mu m$  as indicated by Fig. 3.1.1, thus even though we only have one spatial grid through the vertical direction, the duration of one time step has to be no larger than

$$\Delta t_{\max} = \sqrt{3} \frac{1 \times 10^{-6}}{3 \times 10^8} = 6 \times 10^{-15} s$$

If a time window of  $10^{-9} s$  should be simulated, which corresponds to the  $1GHz$  resonant frequency of the FBAR, the number of time steps is almost one million, which is enormous data. If the spatial

extrapolation (2.3.5) is made, the stability issue is cleverly avoided, and the simulation will be much less time and storage consuming. Therefore, the radiation boundary condition

$$\left. \frac{E_y}{H_x} \right|_{z=h} = -\eta_0 \quad (3.2.8)$$

yields

$$\left. \frac{\partial H_x}{\partial t} = -\frac{1}{\eta_0} \frac{\partial E_y}{\partial t} \right|_{z=h} = -\frac{h}{\eta_0} \frac{\partial E_{y1}}{\partial t} \quad (3.2.9)$$

Substituting (3.2.9) to (3.2.8) gives

$$E_{y1} = \mu_s \frac{\partial H_x}{\partial t} + e_B \frac{\partial v}{\partial z} \quad (3.2.10)$$

Equations (3.2.3), (3.2.5), (3.2.9) and (3.2.10) lead to the leap-frog time-stepping equations for the magnetostrictive layer:

$$\frac{\mu_s h}{\eta_0} \frac{\partial E_{y1}}{\partial t} + E_{y1} = e_B \frac{\partial v}{\partial z} \quad (3.2.11)$$

$$\frac{\partial T}{\partial t} = c_B \frac{\partial v}{\partial z} - \frac{e_B}{\mu_s} E_{y1} \quad (3.2.12)$$

$$\frac{\partial T}{\partial z} = \rho \frac{\partial v}{\partial t} \quad (3.2.13)$$

The leap-frog time-stepping equations for piezoelectric layer are given by (3.2.14) and (3.2.15) following the same procedure.

$$\frac{\partial D}{\partial t} = \varepsilon_s \frac{\partial E_z}{\partial t} + e_D \frac{\partial v}{\partial z} \quad (3.2.14)$$

$$\frac{\partial T}{\partial t} = c_D \frac{\partial v}{\partial z} - \frac{e_D}{\varepsilon_s} \frac{\partial D}{\partial t} \quad (3.2.15)$$

The difference equations in the magnetostrictive layer (3.2.16)–(3.2.18) and in the piezoelectric layer (3.2.19)–(3.2.20) are obtained by discretizing (3.2.11)–(3.2.15) in spatial and temporal

domain.

$$E_{y1}^{n+1/2} = \frac{\frac{\mu_s h}{\eta_0 \Delta t} - 0.5}{\frac{\mu_s h}{\eta_0 \Delta t} + 0.5} E_{y1}^{n-1/2} + \text{mean} \left\{ \frac{e_B}{0.5 + \frac{\mu_s h}{\eta_0 \Delta t}} \frac{v_{i+1/2}^n - v_{i-1/2}^n}{\Delta z} \right\} \quad (3.2.16)$$

$$T_i^{n+1/2} = T_i^{n-1/2} + c_B \frac{v_{i+1/2}^n - v_{i-1/2}^n}{\Delta z} \Delta t - \frac{e_B}{\mu_s} \frac{E_{y1}^{n+1/2} + E_{y1}^{n-1/2}}{2} \Delta t \quad (3.2.17)$$

$$v_{i+1/2}^{n+1} = v_{i+1/2}^n + \frac{\Delta t}{\rho \Delta z} (T_i^{n+1/2} - T_{i-1}^{n+1/2}) \quad (3.2.18)$$

$$T_i^{n+1/2} = T_{i-1}^{n-1/2} + \frac{c_D \Delta t}{\Delta z} (v_{i+1/2}^n - v_{i-1/2}^n) - \frac{e_D}{\epsilon_s} (D_i^{n+1/2} - D_i^{n-1/2}) \quad (3.2.19)$$

$$E_{zi}^{n+1/2} = E_{zi}^{n+1/2} - \frac{e_D \Delta t}{\epsilon_s \Delta z} (v_{i+1/2}^n - v_{i-1/2}^n) + \frac{1}{\epsilon_s} (D_i^{n+1/2} - D_i^{n-1/2}) \quad (3.2.20)$$

A Gaussian electrical excitation  $D(t) = e^{-(t-t_0)^2/2T^2} \cos(2\pi ft)$  is applied through the vertical direction of the bottom piezoelectric layer, which is the input of the recursive FDTD time-marching algorithm.

### 3.2.2. Modeling Results and Analysis

The stress profile (Fig. 3.2.1) of the structure shown in Fig. 3.1.1 is obtained by the proposed FDTD simulation. It represents the radiation of electromagnetic waves acting as a damping load to the acoustic wave resonances, which proves the circuit model in Fig. 2.3.1. Radiation quality factors (Fig. 3.2.2) are derived by extracting the damping speed of the resonances caused by radiation. It shows that a relative permeability of 2000 and a mechanical-to-magnetic figure of merit of greater than 85% in the magnetostrictive material could lead to efficient radiation (with radiation  $Q$  factor of about 100) at 1.03GHz with 1- $\mu m$ -thick magnetostrictive material. The agreement between the numerical solutions and the analytic solutions provides a good validation to both the operating principle of the proposed antenna structure and the FDTD algorithms developed for solving such multi-physics problems.

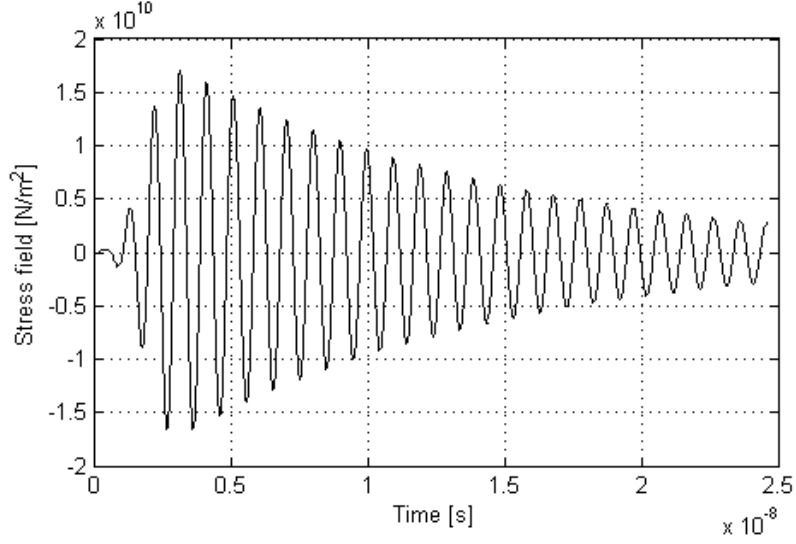
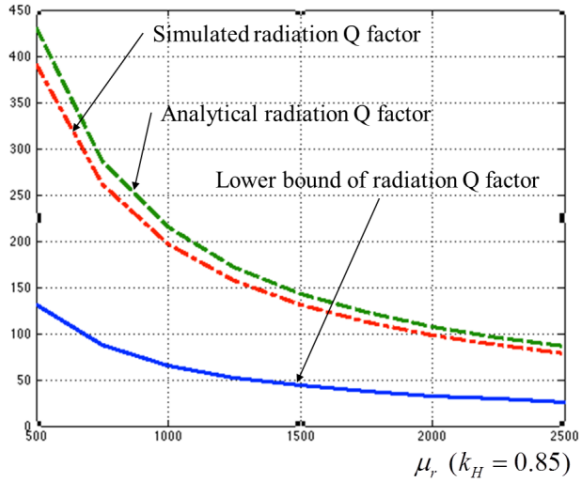
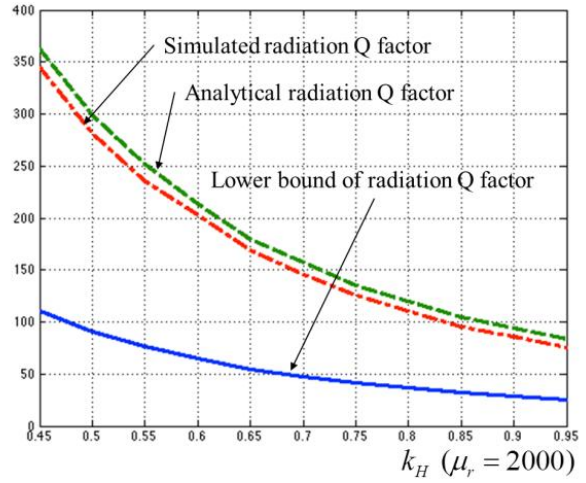


Figure. 3.2.1: Time-domain stress field within the antenna with geometry by Fig. 3.1.1, with ideal nickel with no loss as the magnetostrictive material.  $k_H^2 = 0.91$ ,  $\mu_r = 2000\mu_0$ ,  $s_E = s_H = 2.11e11$  [m²/N],  $\epsilon_s = 10.4\epsilon_0$  [F/m],  $d_E = 1.32$  [C/N],  $d_H = 1.04e-7$  [C/N],  $\rho = 5.68e3$  [kg/m³],  $\sigma = 0$  [S/m]. The frequency is  $f = 1.03GHz$ .



(a)

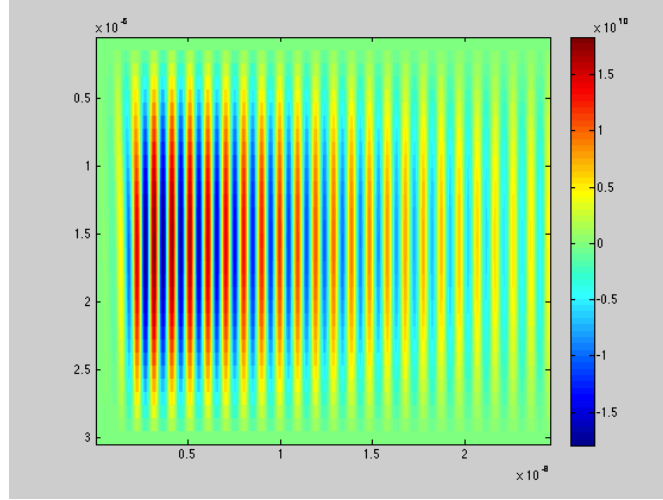


(b)

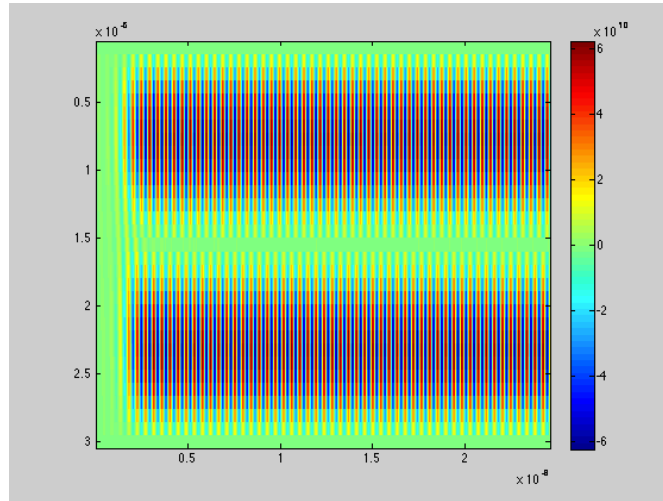
Figure. 3.2.2: (a) Simulated radiation  $Q$  compared to the theory for different permeability,  $k_H = 0.85$ . (b) Simulated radiation  $Q$  compared to the theory for different magnetic to mechanical figure of merits,  $\mu_r = 2000$ . The parameters in Fig. 3.2.1 apply.

In addition, stress profiles within the antenna structure working at different frequencies are generated in Fig. 3.2.3, as a demonstration of the BAW mechanism shown by Fig. 3.1.2. Clearly,

when the total thickness of the structure is  $h_{tot} = \lambda_{acoustic}/2$  and  $h_{tot} = 3\lambda_{acoustic}/2$ , the stress dissipates fast as the radiation into free space acts as a damping load to the FBAR, thus the radiation is maximized. However, when  $h_{tot} = \lambda_{acoustic}$ , the stress does dissipate and there is no electromagnetic radiation. This is a validation of the bulk acoustic wave resonance mechanism that the antenna relies on.

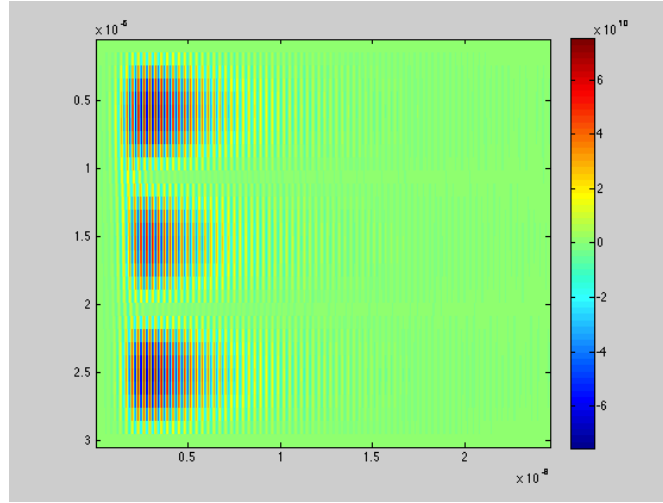


(a)



(b)





(c)

Figure. 3.2.3: Stress profiles inside the proposed antenna structure of Fig. 3.1.1. (a):  $f = 1.03GHz$  , (b)  $f = 2.28GHz$  , (c)  $f = 3.17GHz$  . Horizontal axis: time, 0~2.5e-8s, vertical axis: vertical spatial point of the structure, 0~3 $\mu$ m from top to bottom. The parameters in Fig. 3.2.1 apply.

## CHAPTER 4

### Identification of Loss Effects

The analytical and numerical model we discussed in Chapter 2 and Chapter 3 should be adapted to more realistic case with possible loss factors. Since the radiation is generated by the magnetostrictive layer, the loss should more dominant in this layer than that in the piezoelectric layer. The two main loss factors under consideration in this work are the eddy current loss (electrical conductive loss) and the magnetic damping loss. In this chapter, the previous FDTD modeling will be completed or modified, with losses taken into account.

#### 4.1. Eddy Current Loss

The eddy current loss is identified by adding a conductivity term in the Ampere's law of Maxwell's equations (2.2.1).

$$\nabla \times \bar{H} = \frac{\partial \bar{D}}{\partial t} + \sigma \bar{E} \quad (4.1.1)$$

Following the procedure in Appendix A, we could obtain the time and space difference equations (4.1.2) and (4.1.3), also (A.5) and (A.8). Adapting these two difference equations into Eq. (3.2.16)-(3.2.20) gives the solutions with eddy current loss.

$$E_{y1}^{n+\frac{1}{2}} = \frac{\frac{\varepsilon}{\Delta t} - \frac{\sigma}{2} - \frac{1}{\eta_0 h}}{\frac{\varepsilon}{\Delta t} + \frac{\sigma}{2} + \frac{1}{\eta_0 h}} \cdot E_{y1}^{n-\frac{1}{2}} - \frac{\frac{2}{h^2}}{\frac{\varepsilon}{\Delta t} + \frac{\sigma}{2} + \frac{1}{\eta_0 h}} \cdot H_{x0}^n \quad (4.1.2)$$

$$H_{x0}^{n+1} = \frac{\frac{2\mu^s}{3\Delta t} - \frac{\mu^s}{3\eta_0 h \varepsilon}}{\frac{2\mu^s}{3\Delta t} + \frac{\mu^s}{3\eta_0 h \varepsilon}} H_{x0}^n + \frac{-\frac{2\mu^s}{3\eta_0^2 \varepsilon} - \frac{2\mu^s \sigma h}{3\eta_0 \varepsilon} + 1}{\frac{2\mu^s}{3\Delta t} + \frac{\mu^s}{3\eta_0 h \varepsilon}} E_{y1}^{n+\frac{1}{2}} - \frac{e^B}{\frac{2\mu^s}{3\Delta t} + \frac{\mu^s}{3\eta_0 h \varepsilon}} \text{mean} \left\{ \frac{v_i^{n+\frac{1}{2}} - v_i^{n-\frac{1}{2}}}{\Delta z} \right\} \quad (4.1.3)$$

Fig. 4.1.1 shows the stress profiles with different conductivity values. Energy loss could be indicated by the different damping speed of the stress. As the conductivity increases, the damping speed gets faster, indicating more energy loss due to eddy loss. One should note that the radiated energy remains the same for different conductivity values.

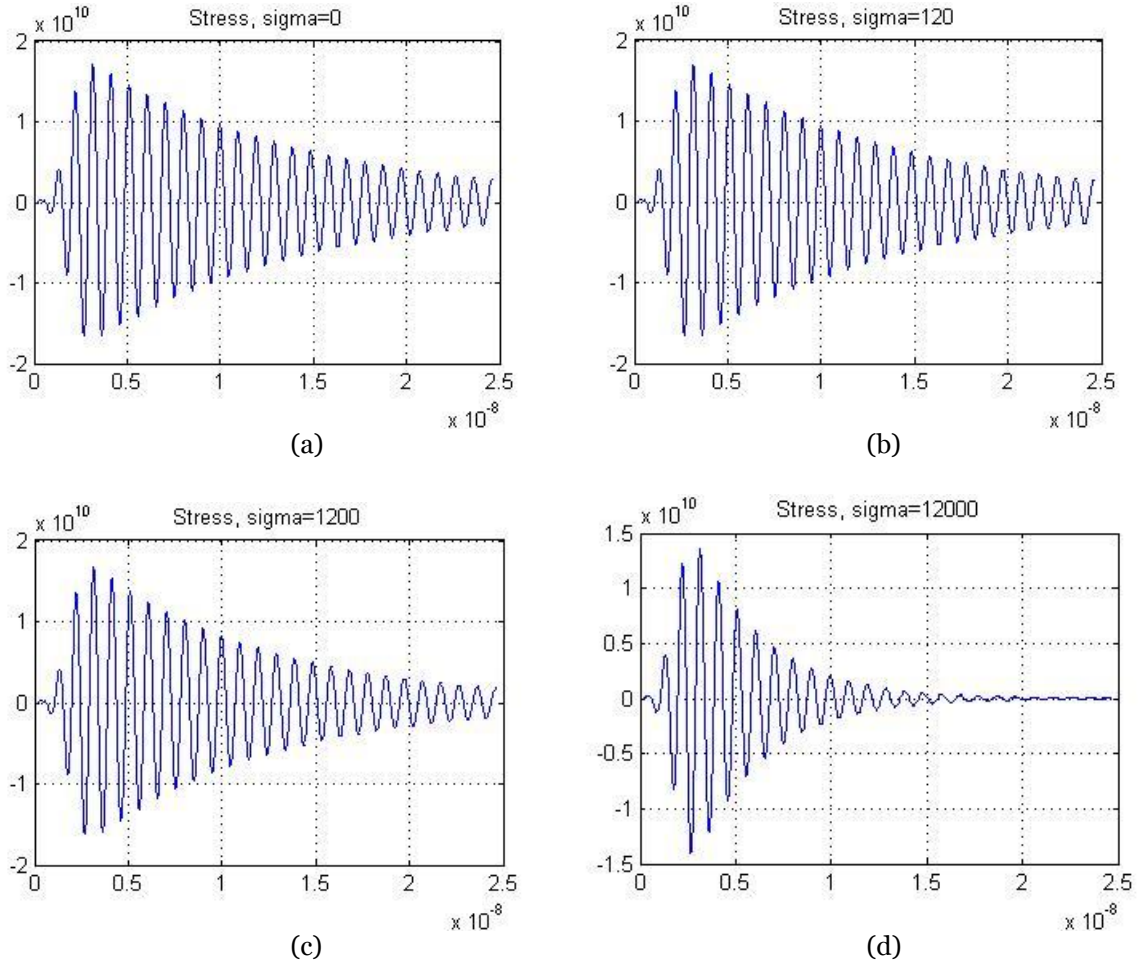


Figure. 4.1.1: Stress curves with different conductivity. (a)  $\sigma = 0$ , (b)  $\sigma = 120 \text{ S/m}$ , (c)  $\sigma = 1200 \text{ S/m}$ , (d)  $\sigma = 12000 \text{ S/m}$ . The parameters in Fig. 3.2.1 apply.

Further evaluation of the eddy loss is done by extracting the quality factors, shown in Table. 4.1.1.

$\sigma$ in S/m	$Q_{bound}$	$Q_{analytical}$	$Q_{simulated}$
$\sigma = 0$	25.6373	84.1951	75.2692
$\sigma = 1.2 \times 10^2$	25.2495	82.9216	73.7001
$\sigma = 1.2 \times 10^3$	22.2711	73.1402	61.4614
$\sigma = 1.2 \times 10^4$	10.2092	33.5277	23.0467

Table. 4.1.1: Quality factors with different conductivities.  $Q_{bound}$  is the radiation quality factor lower bound calculated by  $Q_{bound} = (1/Q_{rad} + 1/Q_{diss})^{-1}$ ,  $Q_{analytical}$  is the analytical radiation quality factor calculated by Eq. (3.1.1),  $Q_{simulated}$  is the simulated total quality factor obtained by the ratio of the phase constant and the attenuation constant.

According to the data in the table, simulated Q factor decreases as conductivity increases, which indicates lower energy stored in the system after the dissipation due to eddy loss. This result is reasonable, according to Eq. (1.1.2); however, low total Q factor does not indicate high radiation anymore; in contrast, it indicates low radiation efficiency. Therefore, low conductivity magnetostrictive materials are preferable for better radiation performance.

## 4.2. Magnetic Damping Loss

### 4.2.1. Modeling Setup

Previous bulk acoustic wave dynamic modeling is based on the assumption of constant relative permeability of the magnetostrictive material, which is an ideal approximation and is not the case in realistic magnetic materials. A more accurate way to model the magnetic material is to utilize the equation of motion of electron spin, also known as Landau-Lifshitz-Gilbert equation (LLG) equation. Similar to the BAW simulation, this dynamic magnetization modeling will also solve the Maxwell's equations and LLG equations simultaneously as both the magnetic moment and electromagnetic coupling phenomena exist physically and inseparably in the ferrite. For the time being, the acoustic factor is removed from the modeling for simplification.

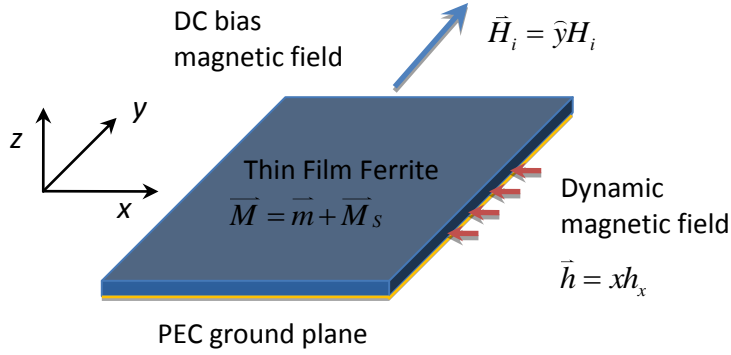


Figure 4.2.1: Problem statement. The ferrite thin film is soft in plane to push the FMR to higher frequency which gives higher initial value of  $\mu'$  since  $\omega_r = \sqrt{\omega_0(\omega_m + \omega_0)} = \sqrt{\chi_0}\omega_0$  where  $\chi_0 = \omega_m/\omega_0 = M_s/H_0$ . A static magnetic field  $\vec{H}_i$  is applied in the  $y$  direction as the DC bias to saturate the ferrite and a dynamic magnetic field excitation is applied in the  $x$  direction. Note that in this section, all the dynamic field components are represented by lower case letters, and the static fields such as the DC bias and saturation magnetization are represented by upper case letters.

The original vector form of the Maxwell and LLG dynamic system is composed of the following equation set as in Eq.(4.2.1)-(4.2.3). Note that Eq. (4.2.2) and (4.2.3) are identical to Eq. (2.2.1).

$$\frac{\partial \vec{M}}{\partial t} = \mu_0 \gamma (\vec{M} \times \vec{H}) - \frac{\alpha}{|\vec{M}|} \vec{M} \times \frac{\partial \vec{M}}{\partial t} \quad (4.2.1)$$

$$\frac{\partial \vec{E}}{\partial t} = \frac{1}{\epsilon_r \epsilon_0} \nabla \times \vec{H} \quad (4.2.2)$$

$$\frac{\partial \vec{B}}{\partial t} = -\nabla \times \vec{E} \quad (4.2.3)$$

In the LLG equation (4.2.1), both gyromagnetic ratio  $\gamma$  and the damping factor  $\alpha$  are negative.

$\gamma = -1.759 \times 10^{-11} \text{ C/kg}$ ,  $\alpha = -0.0065$ . After a lengthy manipulation, the time difference equations are given by Eq. (B.17)-(B.19).

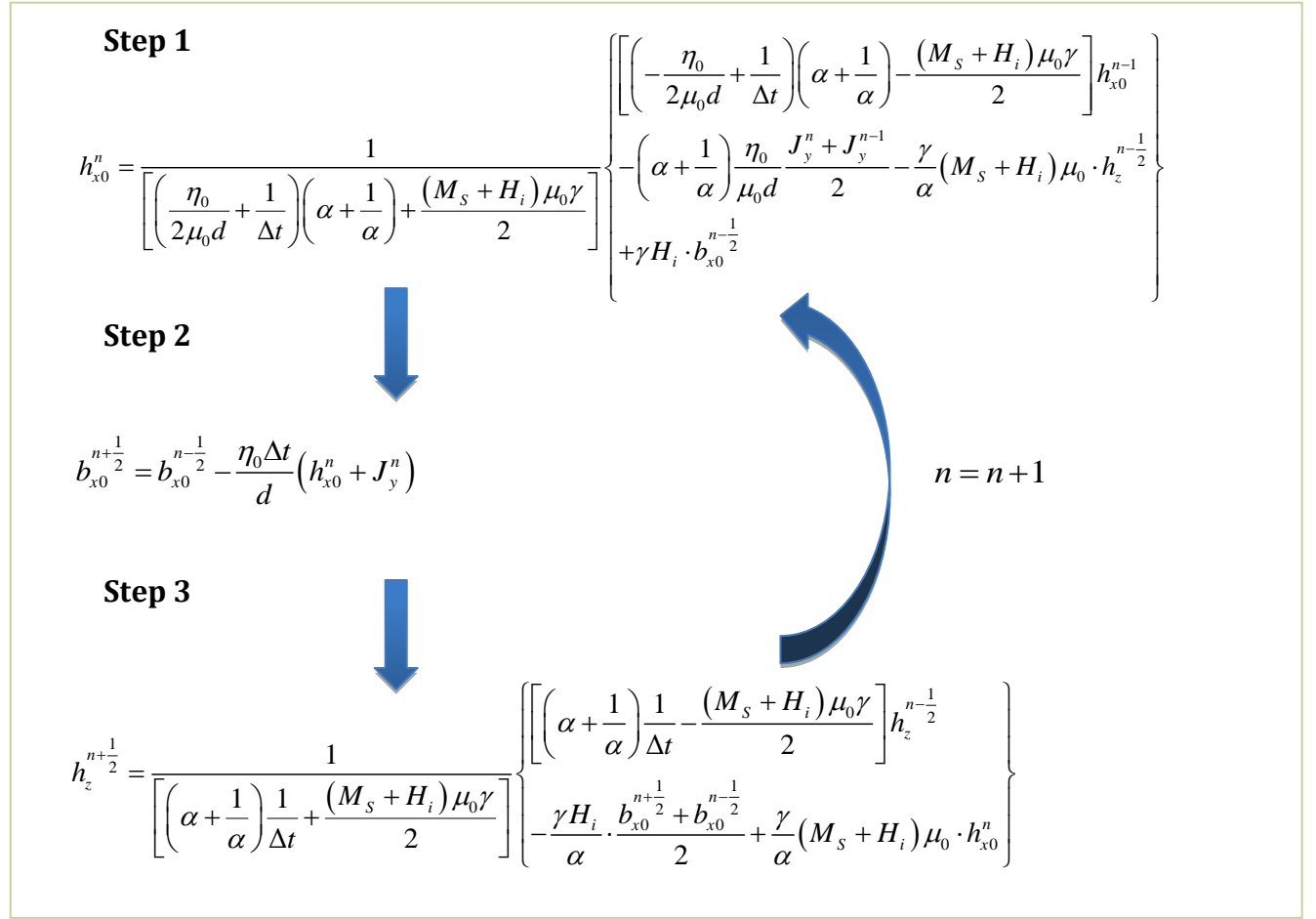


Figure 4.2.2: 1D leap-frogging procedure.

Fig. 4.2.2 shows the 1D leap-frogging procedure. An in-plane excitation of  $J_y = e^{-(t-t_0)^2/2\tau}$  is applied, and the thin film is yttrium iron garnet, with the following properties  $4\pi M_s = 1750 \text{ Gauss}$ ,  $\Delta H = 50 \text{ Oe}$ ,  $\varepsilon_r = 15$ .

### 4.2.2. Modeling Result and Analysis

Both time domain and frequency domain responses of the system are simulated, shown in Fig. (4.2.3)-(4.2.6). The time domain profile of  $b_x$  (Fig. 4.2.3) obviously shows the response of the system, since  $b_x$  still exists even after the original excitation  $J_y$  vanishes.

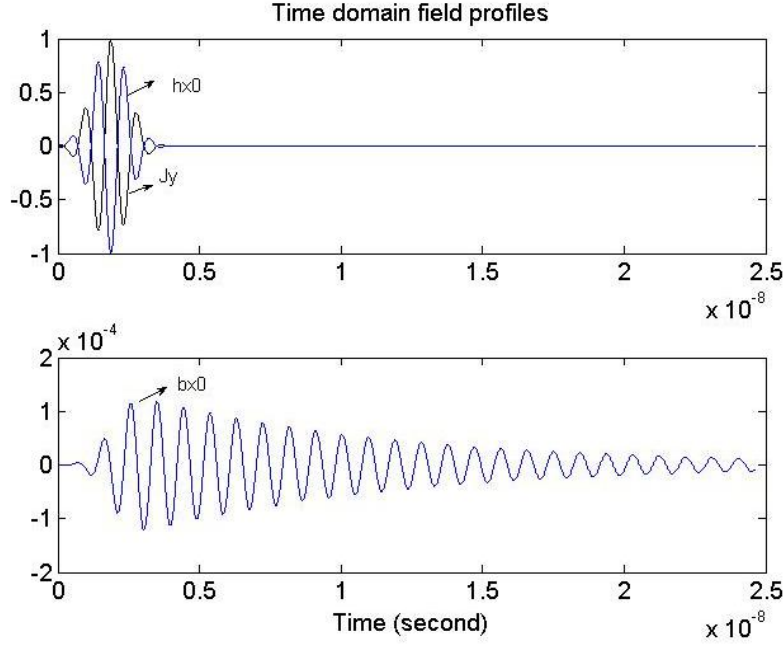


Figure 4.2.3: Time domain field profiles. Note that the time domain profiles are generated with modified Gaussian excitation of  $J_y = e^{-(t-t_0)^2/2\tau} \cos(2\pi ft)$  for clear observation.

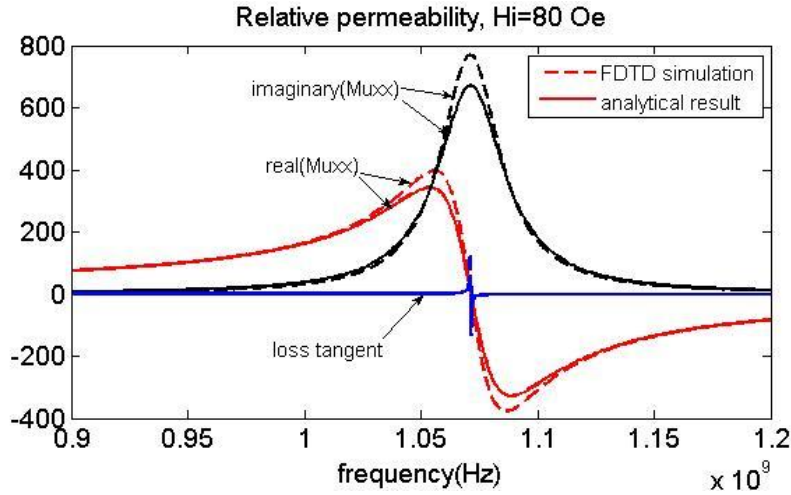


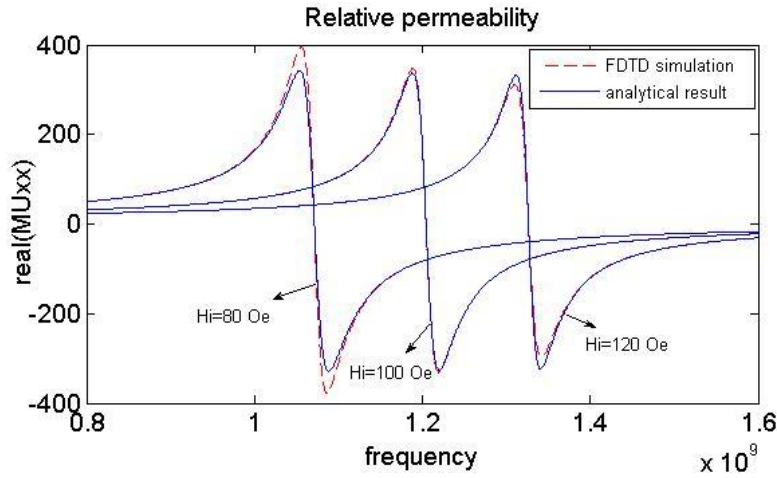
Figure 4.2.4: Relative permeability as a function of frequency. “Muxx” stands for the relative permeability

$\mu_{xx}/\mu_0 = b_x/h_x$ . The analytical expression of thin film FMR is  $\chi = \frac{\omega_m(\omega_m + \omega_0)}{\omega_0(\omega_m + \omega_0) - \omega^2}$ , where

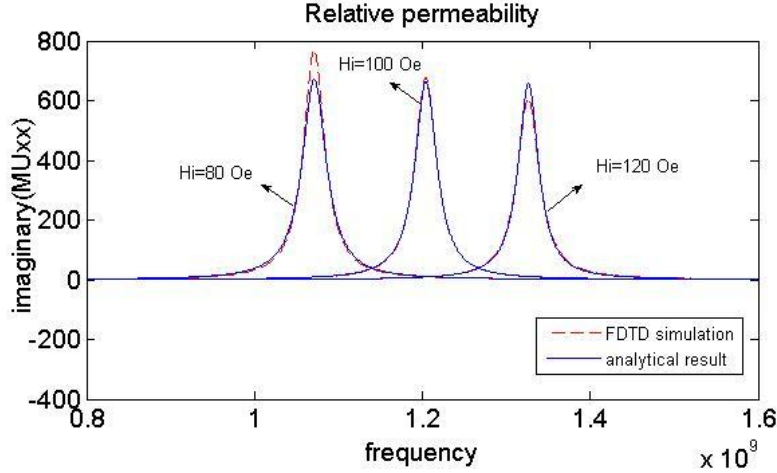
$\omega_0 \leftarrow \omega_0 + j\alpha\omega$  is used with magnetic loss present.

FMR is observed from the simulated curve in Fig. 4.2.4, showing discrepancy from that from

theoretical analysis. This discrepancy is due to the reduction of magnetic field as energy is radiated into free space. Nevertheless, the initial value of  $\mu'$  is approximately 80, and the peak value is 400, which makes YIG a good candidate for the BAW antenna application. FMR shifts to higher frequency as the applied DC bias is increased, as shown in Fig. 4.2.5.



(a)



(b)

Figure 4.2.5: Relative permeability curves with various values of DC bias. (a)  $\mu'$  (b)  $\mu''$ .



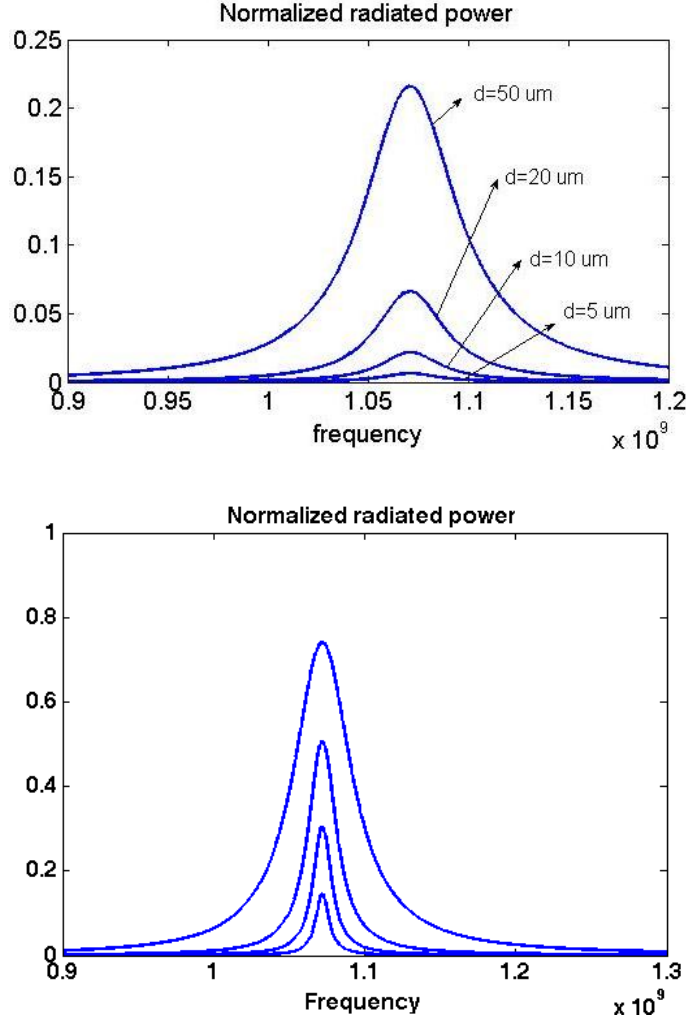


Figure 4.2.6: Normalized radiated power, obtained by  $P_n = \left| \left[ h_{x0}(\omega) + J_y(\omega) \right] / J_y(\omega) \right|^2$ .

Radiated power (Fig. 4.2.6) increases as the thickness of the film increases or the line width of the material decreases. It should be noted that the normalized radiation power is maximum at FMR, where the magnetic loss tangent reaches its peak and the relative permeability is nearly zero. This phenomenon was not predicted prior to this research. It can be explained that near FMR region, the ferrite becomes a good magnetic conductor so that dynamic electromagnetic fields could hardly stand inside the material, which results in high power released into the free space, and thus high power radiation. This conclusion opens up a new antenna design strategy to make the antenna work at FMR to enhance the radiation.

## **CHAPTER 5**

### **CONCLUSION**

#### **5.1. Summary**

Multiferroic antennas can potentially lead high performance antennas with dimensions orders of magnitudes smaller than conventional antennas. High performance ferromagnetic materials with high permeability, low loss tangent, high piezomagnetic coefficients are enabling technology for such applications. Multi-physics and multi-scale simulation tools are being developed and have confirmed such potentials of the proposed antennas.

#### **5.2. Future Work**

Although the working principles and physics have been well studied, the desired material is not available yet. More work should be executed to fabricate the optimum material. In addition, LLG/Maxwell system does not include the acoustic factor; therefore, more complete models are preferred to give accurate prediction of multiferroic radiation. Extension from 1D modeling to 2D and 3D will also be explored as the next step.

# APPENDIX A

## Derivation of the Time Difference Equations with Eddy Loss

Although in the original FDTD modeling without eddy loss, the zeroth order extrapolations (Eq. (2.3.5)) of the magnetic field and magnetic flux density satisfy the coupling equations, when the conductivity of the radiating element is considered, the extrapolated spatial basis function should be:

$$B_x = B_{x0} + B_{x2}z^2, H_x = H_{x0} + H_{x2}z^2, E_y = E_{y1}z \quad (\text{A.1})$$

Eq. (A.1) coupled with the radiation boundary condition  $E_{y1}h/H_{x0} + H_{x2}h^2 = -\eta_0$  reduces to:

$$H_{x2} = -\frac{1}{\eta_0 h} E_{y1} - \frac{1}{h^2} H_{x0} \quad (\text{A.2})$$

The following steps show how to reduce the dynamic differential system into discrete difference equations. Faraday's law gives:

$$\frac{\partial B_x}{\partial t} = \frac{\partial E_y}{\partial z} = E_{y1} \quad (\text{A.3})$$

which coupled with Eq. (A.2) further reduces the Ampere's law  $\nabla \times \vec{H} = \partial \vec{D} / \partial t + \sigma \vec{E}$  to be:

$$\epsilon \frac{\partial E_{y1}}{\partial t} + \left( \sigma + \frac{2}{\eta_0 h} \right) E_{y1} + \frac{2}{h^2} H_{x0} = 0 \quad (\text{A.4})$$

Discretizing Eq. (A.4) gives the time and space difference equation:

$$E_{y1}^{n+\frac{1}{2}} = \frac{\frac{\epsilon}{\Delta t} - \frac{\sigma}{2} - \frac{1}{\eta_0 h}}{\frac{\epsilon}{\Delta t} + \frac{\sigma}{2} + \frac{1}{\eta_0 h}} \cdot E_{y1}^{n-\frac{1}{2}} - \frac{\frac{2}{h^2}}{\frac{\epsilon}{\Delta t} + \frac{\sigma}{2} + \frac{1}{\eta_0 h}} \cdot H_{x0}^n \quad (\text{A.5})$$

Eq. (A.5) is used to update the electric field; however, the magnetic field needs also to be updated, following Eq. (A. 8). The derivation starts with the constitutive coupling (A. 6):

$$\frac{\partial B}{\partial t} = \mu^s \frac{\partial H}{\partial t} + e^B \frac{\partial v}{\partial z}, \quad (\text{A.6})$$

into which (A.2), (A. 3) and (A.4) are substituted to get (A. 7)

$$E_{y1} = \frac{2\mu^s}{3} \frac{\partial H_{x0}}{\partial t} + \frac{2\mu^s}{3\eta_0^2 \varepsilon} E_{y1} + \frac{2\mu^s \sigma h}{3\eta_0 \varepsilon} E_{y1} + \frac{2\mu^s}{3\eta_0 h \varepsilon} H_{x0} + e^B \frac{\partial v}{\partial z} \quad (\text{A.7})$$

Discretizing Eq. (A.7) gives the time and space difference equation:

$$H_{x0}^{n+1} = \frac{\frac{2\mu^s}{3\Delta t} - \frac{\mu^s}{3\eta_0 h \varepsilon}}{\frac{2\mu^s}{3\Delta t} + \frac{\mu^s}{3\eta_0 h \varepsilon}} H_{x0}^n + \frac{-\frac{2\mu^s}{3\eta_0^2 \varepsilon} - \frac{2\mu^s \sigma h}{3\eta_0 \varepsilon} + 1}{\frac{2\mu^s}{3\Delta t} + \frac{\mu^s}{3\eta_0 h \varepsilon}} E_{y1}^{n+\frac{1}{2}} - \frac{e^B}{\frac{2\mu^s}{3\Delta t} + \frac{\mu^s}{3\eta_0 h \varepsilon}} \text{mean} \left\{ \frac{v_i^{n+\frac{1}{2}} - v_i^{n-\frac{1}{2}}}{\Delta z} \right\} \quad (\text{A.8})$$

## APPENDIX B

### Derivation of the Time Difference Equations with Magnetic Damping Factor

Since in this work, the applied DC bias is much larger than the received dynamic EM field, small signal approximation is valid, which states that  $\vec{H}_i \parallel \vec{M}_s$ ,  $\vec{H}_i \perp \vec{m}_{dynamic}$ ,  $m_y \approx 0$ ,  $|M| \approx M_s$ , and all  $hh, bh, bb$  products are ignored. With this approximation, we have

$$\vec{H} = yH_i + h_x x + h_y y + h_z \hat{z} \quad (\text{B.1})$$

$$\vec{M} = \vec{M}_s + \vec{m} = yM_s + xm_x + ym_y + \hat{z}m_z \xrightarrow{m_y=0} yM_s + x\left(\frac{b_x}{\mu_0} - h_x\right) + \hat{z}\left(\frac{b_z}{\mu_0} - h_z\right) \quad (\text{B.2})$$

With small signal approximation shown above, the right-hand side of Eq. (4.2.1) reduces to

$$\begin{aligned} \mu_0 \gamma (\vec{M} \times \vec{H}) &= \mu_0 \gamma \left[ yM_s + x\left(\frac{b_x}{\mu_0} - h_x\right) + \hat{z}\left(\frac{b_z}{\mu_0} - h_z\right) \right] \times \left[ yH_i + xh_x + yh_y + \hat{z}h_z \right] \\ &= \mu_0 \gamma \left[ \begin{aligned} &(-\hat{z})M_s h_x + xM_s h_z + \hat{z}\left(\frac{b_x}{\mu_0} - h_x\right)H_i + \hat{z}\left(\frac{b_x}{\mu_0} - h_x\right)h_y \\ &-y\left(\frac{b_x}{\mu_0} - h_x\right)h_z - x\left(\frac{b_z}{\mu_0} - h_z\right)H_i + y\left(\frac{b_z}{\mu_0} - h_z\right)h_x - x\left(\frac{b_z}{\mu_0} - h_z\right)h_y \end{aligned} \right] \\ &\xrightarrow[\text{small signal approximation}]{\text{ignore all } hh, hb, \text{ and } bb \text{ products}} \mu_0 \gamma \left[ x\left(M_s h_z - \frac{b_z H_i}{\mu_0} + h_z H_i\right) + \hat{z}\left(-M_s h_x + \frac{b_x H_i}{\mu_0} - h_x H_i\right) \right] \\ &= \gamma \left[ x\left(\mu_0 M_s h_z - b_z H_i + \mu_0 h_z H_i\right) + \hat{z}\left(-\mu_0 M_s h_x + b_x H_i - \mu_0 h_x H_i\right) \right] \\ &= -\frac{\alpha}{|M|} \vec{M} \times \frac{\partial \vec{M}}{\partial t} = -\frac{\alpha}{|M|} \left[ yM_s + x\left(\frac{b_x}{\mu_0} - h_x\right) + \hat{z}\left(\frac{b_z}{\mu_0} - h_z\right) \right] \times \frac{\partial}{\partial t} \left[ yM_s + x\left(\frac{b_x}{\mu_0} - h_x\right) + \hat{z}\left(\frac{b_z}{\mu_0} - h_z\right) \right] \\ &\xrightarrow{|M| \approx M_s} -\alpha y \times \frac{\partial}{\partial t} \left[ yM_s + x\left(\frac{b_x}{\mu_0} - h_x\right) + \hat{z}\left(\frac{b_z}{\mu_0} - h_z\right) \right] \\ &= \frac{\alpha}{\mu_0} \left[ \hat{z}(b_x - \mu_0 h_x) - x(b_z - \mu_0 h_z) \right] \end{aligned} \quad (\text{B.4})$$

Combine Eq. (4.2.1), (B.3) and (B.4) all together, the LLG equation reduces to the following scalar form:

$$\frac{1}{\mu_0} \frac{\partial b_z}{\partial t} - \frac{\partial h_z}{\partial t} = \gamma [H_i b_x - \mu_0 (M_s + H_i) h_x] + \alpha \left[ \frac{1}{\mu_0} \frac{\partial b_x}{\partial t} - \frac{\partial h_x}{\partial t} \right] \quad (\text{B.5})$$

$$\frac{1}{\mu_0} \frac{\partial b_x}{\partial t} - \frac{\partial h_x}{\partial t} = \gamma [-H_i b_z + \mu_0 (M_s + H_i) h_z] - \alpha \left[ \frac{1}{\mu_0} \frac{\partial b_z}{\partial t} - \frac{\partial h_z}{\partial t} \right] \quad (\text{B.6})$$

$$b_y = \mu_0 h_y \quad (\text{B.7})$$

Follow the same procedure as introduced by Yee, Eq. (4.2.2) and (4.2.3) reduce to:

$$-\frac{\partial b_x}{\partial t} = \frac{\partial e_z}{\partial y} - \frac{\partial e_y}{\partial z}, \quad -\mu_0 \frac{\partial h_y}{\partial t} = \frac{\partial e_x}{\partial z} - \frac{\partial e_z}{\partial x}, \quad \frac{\partial b_z}{\partial t} = \frac{\partial e_x}{\partial y} - \frac{\partial e_y}{\partial x} \quad (\text{B.8})$$

$$\epsilon_r \epsilon_0 \frac{\partial e_x}{\partial t} = \frac{\partial h_z}{\partial y} - \frac{\partial h_y}{\partial z}, \quad \epsilon_r \epsilon_0 \frac{\partial e_y}{\partial t} = \frac{\partial h_x}{\partial z} - \frac{\partial h_z}{\partial x}, \quad \epsilon_r \epsilon_0 \frac{\partial e_z}{\partial t} = \frac{\partial h_y}{\partial x} - \frac{\partial h_x}{\partial y} \quad (\text{B.9})$$

Enforce the 1D simplification  $\partial/\partial x = \partial/\partial y = 0$  to Eq. (B.8) and (B.9):

$$-\frac{\partial b_x}{\partial t} = -\frac{\partial e_y}{\partial z}, \quad -\mu_0 \frac{\partial h_y}{\partial t} = \frac{\partial e_x}{\partial z}, \quad \frac{\partial b_z}{\partial t} = 0 \quad (\text{B.10})$$

$$\epsilon_r \epsilon_0 \frac{\partial e_x}{\partial t} = -\frac{\partial h_y}{\partial z}, \quad \epsilon_r \epsilon_0 \frac{\partial e_y}{\partial t} = \frac{\partial h_x}{\partial z}, \quad \frac{\partial e_z}{\partial t} = 0 \quad (\text{B.11})$$

Consider both Eq. (B.10) and (B.11), we have the final version of field components relationship:

$$\frac{\partial b_x}{\partial t} = \frac{\partial e_y}{\partial z} = e_{y1}, \quad e_z = 0, \quad b_z = 0 \quad (\text{B.12})$$

The reason that the two equations of  $e_x$  and  $h_y$  are crossed out is that these two equations are decoupled from the dynamic system, thus these two components form an independent plane wave system represented by  $\partial^2 e_x / \partial z^2 - \epsilon_r \epsilon_0 \mu_0 \partial^2 e_x / \partial t^2 = 0$ . Eq. (B.12) simplifies (B.5) and (B.6) to

$$-\frac{\partial h_z}{\partial t} = \gamma [H_i b_x - \mu_0 (M_s + H_i) h_x] + \alpha \left[ \frac{1}{\mu_0} \frac{\partial b_x}{\partial t} - \frac{\partial h_x}{\partial t} \right] \quad (\text{B.13})$$

$$\frac{1}{\mu_0} \frac{\partial b_x}{\partial t} - \frac{\partial h_x}{\partial t} = \gamma [\mu_0 (M_s + H_i) h_z] + \alpha \frac{\partial h_z}{\partial t} \quad (\text{B.14})$$

Note that in the process of deriving (B.12) we made the following extrapolation:

$$e_y = e_{y1} z, \quad h_x = h_{x0} \quad (\text{B.15})$$

to overcome the stability problem.

For 1D simulation, the boundary condition is chosen to be the 1D radiation boundary,

$$\left. \frac{E_y}{H_x} \right|_{z=d} = -\eta_0 \xrightarrow[e_y = e_{y1} z]{\text{linear electric field extrapolation}} \frac{e_{y1} d}{h_{x0} + J_y} = -\eta_0 \Rightarrow e_{y1} = -\frac{\eta_0}{d} (h_{x0} + J_y) \quad (\text{B.16})$$

where  $J_y$  is the surface current excitation. Eq. (B.12)- (B.14) are the finalized differential equations

we use for FDTD coding. But before that, discretization is necessary.

**Step 1:**

$$h_{x0}^n \Leftarrow b_{x0}^{n-\frac{1}{2}}, h_z^{n-\frac{1}{2}}, h_{x0}^{n-1}, J_y^n$$

The core of this step is eliminating  $\partial h_z / \partial t$ .

$$(B.14) \Rightarrow \frac{\partial h_z}{\partial t} = -\frac{\eta_0}{\alpha d \mu_0} (h_{x0} + J_y) - \frac{1}{\alpha} \frac{\partial h_{x0}}{\partial t} - \frac{\gamma \mu_0}{\alpha} (M_s + H_i) h_z$$

Therefore (B.13) reduces to:

$$\begin{aligned} (B.13) &\Rightarrow \frac{\eta_0}{\alpha d \mu_0} (h_{x0} + J_y) + \frac{1}{\alpha} \frac{\partial h_{x0}}{\partial t} + \frac{\gamma \mu_0}{\alpha} (M_s + H_i) h_z = \gamma H_i b_{x0} - \gamma \mu_0 (M_s + H_i) h_{x0} - \frac{\alpha \eta_0}{d \mu_0} (h_{x0} + J_y) - \alpha \frac{\partial h_{x0}}{\partial t} \\ &\Rightarrow \left[ \left( \alpha + \frac{1}{\alpha} \right) \frac{\eta_0}{d \mu_0} + \gamma \mu_0 (M_s + H_i) \right] h_{x0} + \left( \alpha + \frac{1}{\alpha} \right) \frac{\partial h_{x0}}{\partial t} + \left( \alpha + \frac{1}{\alpha} \right) \frac{\eta_0}{d \mu_0} J_y + \frac{\gamma \mu_0}{\alpha} (M_s + H_i) h_z - \gamma H_i b_{x0} = 0 \\ &\xrightarrow{\text{discretize}} \left[ \left( \frac{\eta_0}{2 \mu_0 d} + \frac{1}{\Delta t} \right) \left( \alpha + \frac{1}{\alpha} \right) + \frac{(M_s + H_i) \mu_0 \gamma}{2} \right] h_{x0}^n \\ &= \left[ \left( -\frac{\eta_0}{2 \mu_0 T} + \frac{1}{\Delta t} \right) \left( \alpha + \frac{1}{\alpha} \right) - \frac{(M_s + H_i) \mu_0 \gamma}{2} \right] h_{x0}^{n-1} - \left( \alpha + \frac{1}{\alpha} \right) \frac{\eta_0}{\mu_0 d} \frac{J_y^n + J_y^{n-1}}{2} - \frac{\gamma}{\alpha} (M_s + H_i) \mu_0 h_z^{n-\frac{1}{2}} + \gamma H_i b_{x0}^{n-\frac{1}{2}} \end{aligned} \quad (\text{B.17})$$

**Step 2:**

$$\begin{aligned}
b_{x0}^{n+\frac{1}{2}} &\Leftarrow b_{x0}^{n-\frac{1}{2}}, h_{x0}^n \\
(B.12) &\xrightarrow{\text{discretize}} \frac{b_{x0}^{n+\frac{1}{2}} - b_{x0}^{n-\frac{1}{2}}}{\Delta t} = -\frac{\eta_0}{d} (h_{x0}^n + J_y^n) \\
&\Rightarrow b_{x0}^{n+\frac{1}{2}} = -\frac{\eta_0 \Delta t}{d} [h_{x0}^n + J_y^n] + b_{x0}^{n-\frac{1}{2}}
\end{aligned} \tag{B.18}$$

**Step 3:**

$$h_z^{n+\frac{1}{2}} \Leftarrow b_{x0}^{n+\frac{1}{2}}, h_{x0}^n$$

The core of this step is eliminating  $\partial h_{x0}/\partial t$ .

$$(B.13) \Rightarrow \frac{\partial h_{x0}}{\partial t} = -\frac{\eta_0}{\mu_0 d} (h_{x0} + J_y) - \alpha \frac{\partial h_z}{\partial t} - \gamma \mu_0 (M_s + H_i) h_z$$

Therefore (B.13) reduces to:

$$\begin{aligned}
(B.13) &\Rightarrow -\frac{\partial h_z}{\partial t} = \gamma H_i b_{x0} - \gamma \mu_0 (M_s + H_i) h_{x0} + \alpha \left[ -\frac{\eta_0}{\mu_0 d} (h_{x0} + J_y) + \frac{\eta_0}{\mu_0 d} (h_{x0} + J_y) + \alpha \frac{\partial h_z}{\partial t} + \gamma \mu_0 (M_s + H_i) h_z \right] \\
&\Rightarrow -\frac{\partial h_z}{\partial t} = \gamma H_i b_{x0} - \gamma \mu_0 (M_s + H_i) h_{x0} + \alpha^2 \frac{\partial h_z}{\partial t} + \alpha \gamma \mu_0 (M_s + H_i) h_z \\
&\Rightarrow (\alpha^2 + 1) \frac{\partial h_z}{\partial t} + \alpha \gamma \mu_0 (M_s + H_i) h_z + \gamma H_i b_{x0} - \gamma \mu_0 (M_s + H_i) h_{x0} = 0 \\
&\xrightarrow{\text{discretize}} \Rightarrow (\alpha^2 + 1) \frac{h_z^{n+\frac{1}{2}} - h_z^{n-\frac{1}{2}}}{\Delta t} + \alpha \gamma \mu_0 (M_s + H_i) \frac{h_z^{n+\frac{1}{2}} + h_z^{n-\frac{1}{2}}}{2} + \gamma H_i \frac{b_{x0}^{n+\frac{1}{2}} + b_{x0}^{n-\frac{1}{2}}}{2} - \gamma \mu_0 (M_s + H_i) h_{x0}^n = 0 \\
&\Rightarrow \left[ \frac{(\alpha^2 + 1)}{\Delta t} + \frac{\alpha \gamma \mu_0 (M_s + H_i)}{2} \right] h_z^{n+\frac{1}{2}} = \left[ \frac{(\alpha^2 + 1)}{\Delta t} - \frac{\alpha \gamma \mu_0 (M_s + H_i)}{2} \right] h_z^{n-\frac{1}{2}} - \gamma H_i \frac{b_{x0}^{n+\frac{1}{2}} + b_{x0}^{n-\frac{1}{2}}}{2} + \gamma \mu_0 (M_s + H_i) h_{x0}^n
\end{aligned} \tag{B.19}$$



## REFERENCES

- [1] Z. Yao and Y. Wang, "Dynamic analysis of acoustic wave mediated multiferroic radiation via FDTD methods," *IEEE AP-S & USNC-URSI*, 2014, accepted and to be published.
- [2] J. C.-E. Sten, A. Hujanen, and P. K. Koivisto, "Quality factor of an electrically small antenna radiating close to a conducting plane," *IEEE Trans. Antennas Propag.*, vol. 49, No. 5, May 2001.
- [3] L. J. Chu, "Physical limitations on omni-directional antennas," *J. Appl. Phys.*, vol. 19, pp. 1163-1175, Dec. 1948.
- [4] J. S. McLean, "A re-examination of the fundamental limits on the radiation Q of electrically small antennas," *IEEE Trans. Antennas Propagat.*, vol. 44, No. 5, May 1996.
- [5] R. D. Mindlin, "Electromagnetic radiation from a vibrating quartz plate," *Int. J. Solids Structures*, vol. 9, pp. 697-702, 1973.
- [6] P. C. Y. Lee, "Electromagnetic radiation from an AT-cut quartz plate under lateral-field excitation," *J. Appl. Phys.*, vol. 65, No. 4, pp. 1395-1399, February 1989.
- [7] P. C. Y. Lee, "Electromagnetic radiation from doubly rotated piezoelectric crystal plates vibrating at thickness frequencies," *J. Appl. Phys.*, vol. 67, No. 11, pp. 6633-6642, June 1990.
- [8] R. B. Thompson, "A model for the electromagnetic generation of ultrasonic guided waves in ferromagnetic metal polycrystals," *IEEE Trans. Sonics Ultrason.*, vol. SU-25, No. 1, pp. 7-15, January 1978.
- [9] K. S. Yee, "Numerical solutions of initial boundary value problems involving Maxwell's equations in isotropic media," *IEEE Trans. Microw. Theory Techn.*, vol. AP-14, No. 8, pp. 302-307, May 1966.
- [10] K. Seo, S. Ju, and H. Kim, "The modeling of thin-film bulk acoustic wave resonators using the FDTD methods," *IEEE Electron Device Lett.*, vol. 23, pp. 327-329, June 2002.
- [11] D. M. Pozar, "Microstrip Antennas," *Proc. IEEE*, vol. 80, No. 1, pp. 79-81, January 1992.
- [12] H. Schmid, "Multiferroic magnetoelectrics," *Ferroelectrics*, 162, 317-338, 1994.

- [13] L. W. Martin, S. P. Crane, Y-H Chu, M. B. Holcomb, M. Gajek, M. Huijben, C-H Yang, N. Balke and R. Ramesh, “Multiferroics and magnetoelectrics: thin films and nanostructures,” *J. Phys.: Condens. Matter* 20, 2008.
- [14] N. A. Hill, “Why are there so few magnetic ferroelectrics,” *J. Phys. Chem. B*, Vol. 104, No. 29, pp. 6694, 2000.
- [15] A. F. Vaz, J. Hoffman, C. H. Ahn, and R. Ramesh, “Magnetoelectric coupling effects in multiferroic complex oxide composite structures,” *Adv. Mater.*, vol. 22, pp. 2900–2905, 2010.
- [16] L. Mitoseriu, V. Buscaglia, “Intrinsic/extrinsic interplay contributions to the functional properties of ferroelectric-magnetic composites,” *Phase Transitions*, vol. 79, No. 12, pp. 1095–1121, December 2006.
- [17] B. A. Auld, “Piezoelectricity,” in *Acoustic Fields and Waves in Solids*, 2nd ed. Malabar: Krieger Publishing Company, Inc., 1990, ch. 8, sec. F, pp. 281–282.